





# The evolutionary history of GD 1400AB, a white dwarf–brown dwarf binary

S. L. Casewell <sup>1</sup>★, M. R. Burleigh,<sup>1</sup> R. Napiwotzki,<sup>2</sup> M. Zorotovic <sup>3</sup>, P. Bergeron,<sup>4</sup> J. R. French <sup>1</sup>, J. Hermes <sup>5</sup>, F. Faedi<sup>1</sup> and K. L. Lawrie<sup>1</sup>

<sup>1</sup>*School of Physics and Astronomy, University of Leicester, University Road, Leicester LE1 7RH, UK*

<sup>2</sup>*Centre for Astrophysics Research, STRI, University of Hertfordshire, College Lane, Hatfield AL10 9AB, UK*

<sup>3</sup>*Instituto de Física y Astronomía, Universidad de Valparaíso, Av. Gran Bretaña 1111, Valparaíso, Chile*

<sup>4</sup>*Département de Physique, Université de Montréal, C.P. 6128, Succ. Centre-Ville, Montréal, QC H3C 3J7, Canada*

<sup>5</sup>*Department of Astronomy & Institute for Astrophysical Research, Boston University, 725 Commonwealth Avenue, Boston, MA 02215, USA*

Accepted 2024 October 2. Received 2024 September 23; in original form 2024 August 6

## ABSTRACT

GD1400AB was one of the first known white dwarf + brown dwarf binaries and is the only one of these systems where the white dwarf is a ZZ Ceti pulsator. Here, we present both radial velocity measurements and time-series photometry, analysing both the white dwarf pulsations and the effects of irradiation on the brown dwarf. We find that the brightness temperatures of  $1760 \pm 10$  K for the nightside and  $1860 \pm 10$  K for the dayside indicate that the brown dwarf is hotter than spectra have previously suggested, although brightness temperatures calculated using a larger radius for the brown dwarf are consistent with previously determined spectral types. We also discuss the likely evolutionary pathway of this binary and put its common envelope phase into context with the other known systems.

**Key words:** brown dwarfs – stars: low-mass – white dwarfs – infrared: stars.

## 1 INTRODUCTION

Detached brown dwarf + white dwarf systems allow the exploration of a variety of aspects of binary formation and evolution, including probing the known deficit of brown dwarf companions to main-sequence stars (McCarthy & Zuckerman 2004; Grether & Lineweaver 2006; Metchev & Hillenbrand 2009). In detached systems (close or wide), the brown dwarfs themselves can be studied spectroscopically because they dominate the spectral energy distribution at near- to mid-infrared (IR) wavelengths (Farihi & Christopher 2004; Dobbie et al. 2005; Burleigh et al. 2006a; Casewell et al. 2018b, 2020a; Lew et al. 2022; Zhou et al. 2022). It should be noted that there are few observational constraints on brown dwarf evolutionary models at older ages, such as might be expected for most white dwarfs ( $>1$  Gyr; Pinfield et al. 2006) as determining the age of a field brown dwarf is challenging due to the age–mass–radius–luminosity degeneracy.

The closest brown dwarf + white dwarf pairs provide another channel for cataclysmic variable (CV) formation (Politano 2004; Burleigh et al. 2006b; Littlefair et al. 2007; Hernández Santisteban et al. 2016), in which the substellar companion survives common envelope (CE) evolution when it is engulfed by the envelope of the red giant progenitor to the white dwarf (Maxted et al. 2006; Parsons et al. 2017; Rappaport et al. 2017). *In extremis*, the closest such binaries might even represent the end state of CV evolution,

in which the secondary has become highly evolved through mass transfer (Patterson, Thorstensen & Kemp 2005). Indeed, Zorotovic & Schreiber (2022) calculated the CE efficiency for the known white dwarf + brown dwarf pairs to be  $0.24 \leq \alpha_{\text{CE}} \leq 0.41$ , which is consistent for CVs with main-sequence secondary stars.

In close detached binaries, the brown dwarf is irradiated by the high ultraviolet flux of the white dwarf, leading to substantial temperature differences between the ‘day’ and ‘night’ hemispheres. Such systems can provide empirical laboratories for comparison with models for irradiated ‘hot Jupiter’ atmospheres (Fortney et al. 2008; Knutson et al. 2012; Stevenson et al. 2014; Arcangeli et al. 2019; Beatty et al. 2019; Mikal-Evans et al. 2022). However, detached brown dwarf companions to white dwarfs are rare (the fraction of L-type secondaries is  $<0.5$  per cent; Farihi, Becklin & Zuckerman 2005b; Girven et al. 2011; Steele et al. 2011) with only  $\sim 20$  such systems known to date, of which  $\sim 10$  are close, post-CE binaries, although many candidates are known (Brown et al. 2023). The majority of these systems studied to date have been those in which the brown dwarf is highly irradiated: WD0137–349B (Casewell et al. 2015; Longstaff et al. 2017; Lee et al. 2020; Zhou et al. 2022), SDSS1411 (Casewell et al. 2018b; Lew et al. 2022), and EPIC212235321 (Casewell et al. 2018a; Lothringer & Casewell 2020; Zhou et al. 2022). These three systems have periods between 68 min and  $\sim 2$  h, and the white dwarfs have effective temperatures between 25 000 and 13 000 K. Very little is known as to the effects of irradiation on brown dwarfs orbiting cooler white dwarf primaries, although what is known suggests that some form of inflation of the brown dwarf is likely (e.g. Casewell et al. 2020a, b). The majority of these

\* E-mail: [slc25@leicester.ac.uk](mailto:slc25@leicester.ac.uk)

close binaries have periods of  $\sim 2$  h (e.g. Maxted et al. 2006; Steele et al. 2013; Littlefair et al. 2014; Casewell et al. 2020a), making those with longer periods unusual: GD 1400AB at  $\sim 10$  h (Burleigh et al. 2011) and ZTFJ0038+2030 with a period of 10.36 h (van Roestel et al. 2021). The only post-CE systems known with substellar companions and long orbital periods are Gaia 0007–1605, which has a period of 1.0446 d (Rebassa-Mansergas et al. 2022), and the white dwarf–planet system WD1856+534Ab, which has a period of 1.407 d (Vanderburg et al. 2020).

GD 1400 (WD0145–221) is a DA white dwarf located at  $46.25 \pm 0.07$  pc. Farihi & Christopher (2004) determined that GD 1400 had a likely unresolved L dwarf companion, confirmed as an L7 dwarf with near-IR spectroscopy by Dobbie et al. (2005). Farihi, Zuckerman & Becklin (2005a) subsequently obtained *Spitzer* InfraRed Array Camera (IRAC) photometry from 3.6 to 9 microns, which was also consistent with a secondary of L5–L7 spectral type. The most recent work on the system was by Walters et al. (2023), who determined an effective temperature of 2100 K for the brown dwarf, significantly hotter than suggested by the previous spectra. GD 1400 is known to be a ZZ Ceti pulsator; hence, it is photometrically variable with Fontaine et al. (2003), Kilkenny et al. (2014), and Bognár et al. (2020) detecting numerous periods.

In this paper, we present radial velocity (RV) measurements and time-series photometry of the GD 1400 system in order to better constrain the mass of the brown dwarf, likely levels of irradiation, and the effects the pulsations are having on the system. We also present an in-depth analysis of the likely CE evolution of the system, and how this compares to other binaries formed via the same evolutionary pathway.

## 2 GD 1400A

Gentile Fusillo et al. (2021) fitted the *Gaia* photometry and parallax of GD 1400A with pure hydrogen atmosphere models and obtained an effective temperature of  $T_{\text{eff}} = 11\,090 \pm 160$  K and a surface gravity of  $\log g = 8.00 \pm 0.03$ , resulting in a mass of  $0.604 \pm 0.016 M_{\odot}$ . This is broadly consistent with the values given in Koester et al. (2009) of  $T_{\text{eff}} = 11\,747 \pm 20$  K and  $\log g = 8.066 \pm 0.007$  from spectroscopy alone. A more recent spectroscopic determination by Bergeron et al. (2021) yields a slightly higher mass with parameters of  $T_{\text{eff}} = 11\,390 \pm 260$  K,  $\log g = 8.17 \pm 0.19$ , and a mass of  $0.71 \pm 0.06 M_{\odot}$ , although the spectrum in this case is a classification spectrum from the Montreal–Cambridge–Tololo survey. Walters et al. (2023) determined parameters of  $T_{\text{eff}} = 11\,000 \pm 500$  K and a mass of  $0.59 \pm 0.07 M_{\odot}$  based on the *Gaia* Data Release 3 (DR3) parallax and the Pan-STARRS photometry.

Vincent, Bergeron & Lafrenière (2020, see their fig. 4) show the difference between spectroscopically and photometrically derived parameters for ZZ Ceti stars, highlighting the fact that time-averaged photometry of ZZ Ceti pulsators is not the same as for non-pulsating DA white dwarfs. The lack of a *u*-band measurement for GD1400A would also likely bias the photometric fit towards lower effective temperatures (Bergeron et al. 2019). We decided to independently measure the parameters of GD 1400A by reanalysing the best available photometric and spectroscopic data available. We show in Fig. 1 our photometric fit to GD 1400A using the *Gaia* parallax, *Galaxy Evolution Explorer* (GALEX), Pan-STARRS *grizy*, and 2 micron all sky survey (2MASS) photometry. In doing so, however, we exclude the photometric passbands that appear contaminated by the brown dwarf companion. We obtain  $T_{\text{eff}} = 12\,169 \pm 50$  K,  $\log g = 8.14 \pm 0.06$ , and  $M = 0.689^{+0.006}_{-0.004} M_{\odot}$ .

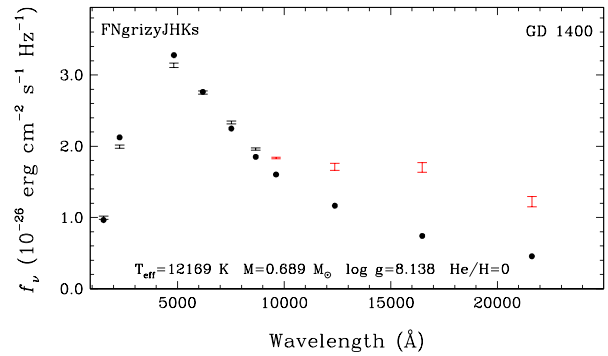


**Figure 1.** Our best fit to the photometry from *GALEX*, Pan-STARRS, and 2MASS (shown by error bars), and using the *Gaia* DR3 parallax. Filled circles represent the best-fitting model with parameters given in the panel. The red error bars correspond to the photometric data not included in the fit as they are in photometric excess over the single white dwarf model.

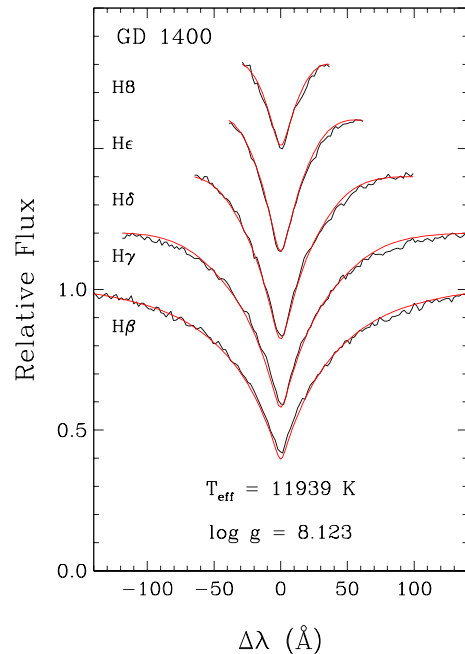


**Figure 2.** Spectroscopic fit to the normalized Balmer lines of GD 1400A.

We also updated the spectroscopic fit using the optical spectrum from Gianninas, Bergeron & Ruiz (2011) with the most recent DA white dwarf models, and by including the 3D hydrodynamical corrections from Tremblay et al. (2013). We rely on the evolutionary models from Bédard et al. (2020) with CO cores,  $q(\text{He}) \equiv \log M_{\text{He}}/M_{*} = 10^{-2}$ , and  $q(\text{H}) = 10^{-4}$ , which are representative of H-atmosphere white dwarfs. Our best fit displayed in Fig. 2 is obtained with  $T_{\text{eff}} = 11\,939 \pm 177$  K and  $\log g = 8.123 \pm 0.046$ , which result in a mass of  $M = 0.680 \pm 0.029 M_{\odot}$ , in excellent agreement with our photometric solution. This updated mass gives a gravitational redshift of  $35 \text{ km s}^{-1}$ , larger than the measured difference in  $\gamma$  velocities given in Walters et al. (2023), but broadly consistent with the gravitational redshift for their adopted mass.

We can estimate an upper limit on the total age of the system using the white dwarf cooling age, the initial–final mass relation (IFMR) for white dwarfs and an estimate of the main-sequence lifetime,

neglecting any accelerated evolution during the CE phase. Using the software `WDWARFDATE` (Kiman et al. 2022) and with the Cummings et al. (2018) IFMR and MESA Isochrones and Stellar Tracks (MIST) isochrones, we determine the cooling age to be  $0.46^{+0.04}_{-0.03}$  Gyr and the white dwarf progenitor mass to be  $2.09^{+0.49}_{-0.52} M_{\odot}$ . The total system age is estimated to be  $1.76^{+1.20}_{-0.56}$  Gyr. It should, however, be noted that this is an upper limit, as we do not know when the main-sequence lifetime of the white dwarf progenitor was truncated by the CE evolution.

### 3 RADIAL VELOCITY OBSERVATIONS

15 high-resolution optical spectra of GD 1400 were obtained between 2006 July and September with the Ultraviolet and Visible Echelle Spectrograph (UVES; Dekker et al. 2000) on UT2 of the European Southern Observatory’s Very Large Telescope (ESO VLT), under programme 077.D-0673(A). UVES was used with the DIC-1 dichroic, with the split beams centred at 3900 and 5640 Å, giving a resolution of 0.04 Å and an RV accuracy of  $1.5 \text{ km s}^{-1}$  in the cores of the H  $\alpha$  and H  $\beta$  absorption lines. The observations were performed in service mode, in seeing no worse than 1.4 arcsec, for a total exposure time of 1200 s to deliver an anticipated  $S/N \approx 25 \text{ pixel}^{-1}$  (using  $2 \times 2$  binning). Each observation was split into  $2 \times 600$  s exposures to avoid smearing.

The spectra were reduced with the ESO MIDAS pipeline for UVES, in the same way as for the ESO Supernova Type 1 Survey (Napiwotzki et al. 2020) including the merging of the Echelle orders and the wavelength calibration. The quality of these automatically extracted spectra is very good, except for a quasi-periodic wave-like pattern that occurs in some of the spectra. This is largely removed by additional processing. In addition, a featureless (DC) white dwarf, WD0000–345, was observed as part of the programme to aid in correcting the detector response curve.

We see no sign of emission within the Balmer features at any phase that could be caused by irradiation (e.g. Longstaff et al. 2017), which was expected as no such emission is seen in the lines of WD1032+011 (Casewell et al. 2020a), which has a similar white dwarf temperature, but a 2 h period.

We measured the RVs of GD 1400 from the non-local thermodynamic equilibrium (NLTE) line cores of the Balmer lines H  $\alpha$  and H  $\beta$ . The measurements were carried out with the package FITSB2 designed to fit the spectra of single-lined (SB1) and double-lined (SB2) binaries (Napiwotzki et al. 2004) as for Napiwotzki et al. (2020).

Synthetic spectra from Koester (2010) were convolved to the observational resolution with a Gaussian and interpolated to the actual parameters with bi-cubic splines and interpolated to the observed wavelength scale. We used the model profiles computed by Koester et al. (1998) for their investigation of rotation in white dwarfs. These are computed performing an NLTE line formation on top of up-to-date local thermodynamic equilibrium model atmospheres for DA white dwarfs (Koester et al. 1998) for details. The inner core of GD 1400 is not very well reproduced by the model profiles. The very likely explanation of this is GD 1400 being a large-amplitude ZZ Ceti variable. FITSB2 offers the option to combine model spectra with other line profiles. In our case, we achieved reasonable representation of the observed line profile by adding a central Gaussian component.

The line profiles were derived from a simultaneous fit of all spectra available, significantly reducing the overall uncertainties. The RV errors were determined by bootstrapping the pixels of the spectra (see Napiwotzki et al. 2020). We determined an RV dispersion of  $\sigma_{RV} = 0.71 \text{ km s}^{-1}$ , indicating very good stability for the observations. Any

RV shifts seen within the measurements are likely caused by the ZZ Ceti pulsations (Berger et al. 2005).

The period search was carried out by means of a periodogram method (see Lorenz, Mayer & Drechsel 1998; Napiwotzki et al. 2001). Sine-shaped RV curves were fitted to the measured RVs for a large range of trial periods. The quality of each fit was determined based on the sum of the squared residuals ( $\chi^2$ ). A detailed fit for the best period estimate was then done to derive the orbital semi-amplitude  $K_1$ , system velocity  $\gamma_1$ , and the epoch of phase zero  $T_0$ . The last one is defined here as the conjunction time when the visible primary moves from the blue side to the red side of the RV curve.

The orbital parameters were then refined by fitting with FITSB2 using the solution from above as starting point. In this process, we fit all spectra simultaneously leading to a direct determination of the orbital parameters (and line profile parameters), with the errors estimated using the bootstrapping method. However, there exists no straightforward way to include the systematic errors affecting complete spectra in this error estimate, and so we used an alternative approach: the bootstrapping is applied to the set of spectra, instead of pixels within the spectra. For each bootstrapping step, a list with a random selection of spectra is produced and a fit is performed exactly the same way it is done on the original set of spectra. This is repeated several times (we used 2000 iterations) and error estimates are computed from the scatter of the fitted parameters. As long as ‘systematic’ errors vary in a random way between spectra – which is likely true for most error sources, e.g. centroiding errors or not perfectly corrected flexing of the spectrograph – these are fully taken into account (Table 1: Fig 3).

To take into account that it is possible that the correct period is very different from the best-fitting period, for instance, outside the formal error limits, we converted the  $\chi^2$  values fitted for the trial periods into probabilities before integrating over the periods – comparing the probability for an interval centred on the primary peak with the ‘outside’ region. The integration was carried out between 0.1 and 30 d extending over all plausible periods for this post-CE system.

## 4 TIME-SERIES PHOTOMETRY

### 4.1 Optical wavelength

As GD 1400A is a ZZ Ceti variable, we monitored it between 2007 and 2010 at the South African Astronomical Observatory (SAAO) with the STE4 CCD imager and the UCT high-speed camera mounted on the 1.0 m telescope in white light (i.e. with no filter). The data were reduced using SAAO’s data reduction pipeline, which subtracted the bias, flat-fielded the science frames, and extracted the brightness of the stars in the frames using DAOPHOT. The light curve is expressed in terms of flux relative to the average brightness of the star. In some cases, a low-order, best-fitting polynomial was also subtracted from the light curve to remove any residual extinction effects. A summary of the observations is given in Table 2 and an example of the light curves from 2010 is shown in Fig. 4, where the multiperiodic nature of the variable is clearly evident. Observations taken during the same run were combined into a single epoch light curve and analysed using the Period04 program (Lenz & Breger 2005). The Fourier transform (FT) of each epoch is illustrated in Fig. 5, along with its window function and prewhitened FT, obtained from subtracting the best-fitting periodicities from the light curve and recalculating the FT. Table 3 summarizes the best-fitting periodicities determined from non-linear least-squares fitting for the 2007, 2008, 2009, and 2010 data sets, with both least-squares and Monte Carlo uncertainties computed using Period04. We have not attempted to

**Table 1.** Spectroscopic orbit of GD 1400A and adopted parameters.

Parameter	Value
$P$ (d)	$0.415\,82 \pm 0.000\,08$
$T_0$ (BJD)	$2451699.888265 \pm 0.001128$
$K_1$ (km s $^{-1}$ )	$24.08 \pm 0.96$
$\gamma_1$ (km s $^{-1}$ )	$42.11 \pm 0.59$
$T_1$ (K)	$11\,939 \pm 180$ K
$M_1$ ( $M_\odot$ )	$0.680 \pm 0.029$
$M_2 \sin i$ ( $M_\odot$ )	$78 \pm 6 M_{\text{Jup}}$

**Table 2.** Journal of SAAO time-series photometric observations.

Telescope/instrument	Observation date (UTC)	Start time (UTC)	Exposure time (s)	Number of points
SAAO 1.0 m STE4	2007-11-30	19:50:13	12	480
SAAO 1.0 m STE4	2007-12-03	20:18:45	12	140
SAAO 1.0 m STE4	2007-12-04	21:06:52	12	287
SAAO 1.0 m UCT	2008-10-31	18:21:50	10	1815
SAAO 1.0 m UCT	2008-11-04	18:35:59	10	451
SAAO 1.0 m UCT	2009-10-30	22:21:46	10	1438
SAAO 1.0 m UCT	2009-10-31	18:31:52	10	876
SAAO 1.0 m UCT	2009-11-04	20:55:02	10	1106
SAAO 1.0 m UCT	2010-09-29	20:42:01	10	1325
SAAO 1.0 m UCT	2010-10-17	19:18:37	10	1817
SAAO 1.0 m UCT	2010-10-18	19:08:50	10	1400
SAAO 1.0 m UCT	2010-10-26	18:59:28	10	1437

identify multiplets or  $\ell$ ,  $k$ , and  $m$  modes and the orbital period of GD 1400AB at  $\sim 10$  h is not detected in these data. All phases of the orbital period have been covered with the light curve, but we also find no indication of an eclipse when the light curve is folded on the orbital period.

Tentative periods were identified by Fontaine et al. (2003) at 462.20, 727.90, and 823.20 s in data taken in July 2002 at the 3.6 m Canada–France–Hawaii Telescope with LAPOUNE, a portable Montréal three-channel photometer. In 2012, Kilkeny et al. (2014) determined periods of 437, 730, and 454 s in order of dominance, two of which are consistent with those determined by Fontaine et al. (2003). Bognár et al. (2020) used 13 448 data points from NASA’s Transiting Exoplanet Survey Satellite (TESS) sector 3 in 120 s mode over 20.3 d to determine periods of 415.420 s with the second highest peaks at 451 s consistent with previous work. At lower frequencies, there were clusters of periods around 1046, 796, and 766 s detected, all of which are complex (below frequencies  $\sim 1400$   $\mu\text{Hz}$ ). They also comment that there could be a ‘triplet’ of frequencies at  $\sim 765$  s leading to a rotation period of either 3.3 or  $\sim 0.57$  d, although the authors were unable to confirm this. When TESS returned to Southern hemisphere observations, it was found by Bognár et al. (2023) that the detected pulsation periods had changed.

We also detect three significant frequencies, 1395.9763 (at 716.34 s), 1413.0393, and 1370.4765  $\mu\text{Hz}$ . However, if those are from splitting caused by the rotation period, they are uneven – 17.1 and 25.5  $\mu\text{Hz}$  from the central component, respectively. At these periods, the mode density also increases, leading to overlapping  $\ell = 1$  and  $\ell = 2$  modes making identification of triplets challenging.

GD 1400 sits in a typical place within the ZZ Ceti instability strip (Hermes et al. 2017); however, the best-fitting periodicities are not stable, with the peak frequencies and amplitudes changing from year to year. Unfortunately, this makes GD 1400A an unsuitable candidate for a long-term O–C study to search for tertiary, lower mass

**Table 3.** Best-fitting periodicities for each epoch of data (also marked on the FTs in Fig. 5). Both formal least-squares uncertainties and italicized Monte Carlo uncertainties, as computed using Period04, are given.

Year		Frequency ( $\mu\text{Hz}$ )	Period (s)	Amplitude (mma)
2007	<b>1:</b>	$1613.126 \pm 0.032$ <i><math>\pm 0.041</math></i>	$619.914 \pm 0.012$ <i><math>\pm 0.016</math></i>	$26.14 \pm 0.85$ <i><math>\pm 0.98</math></i>
	<b>2:</b>	$2172.433 \pm 0.058$ <i><math>\pm 7.514</math></i>	$460.313 \pm 0.012$ <i><math>\pm 1.593</math></i>	$14.58 \pm 0.85$ <i><math>\pm 1.62</math></i>
	<b>3:</b>	$1389.348 \pm 0.177$ <i><math>\pm 8.420</math></i>	$719.762 \pm 0.092$ <i><math>\pm 4.363</math></i>	$10.53 \pm 0.92$ <i><math>\pm 3.22</math></i>
	<b>4:</b>	$3797.264 \pm 0.092$ <i><math>\pm 16.074</math></i>	$263.348 \pm 0.007$ <i><math>\pm 1.115</math></i>	$9.24 \pm 0.84$ <i><math>\pm 1.88</math></i>
	<b>5:</b>	$1203.470 \pm 0.099$ <i><math>\pm 59.798</math></i>	$830.931 \pm 0.069$ <i><math>\pm 41.390</math></i>	$8.74 \pm 0.85$ <i><math>\pm 1.93</math></i>
2008	<b>1:</b>	$2176.060 \pm 0.038$ <i><math>\pm 0.040</math></i>	$459.546 \pm 0.008$ <i><math>\pm 0.009</math></i>	$26.62 \pm 0.64$ <i><math>\pm 0.63</math></i>
	<b>2:</b>	$1307.978 \pm 0.060$ <i><math>\pm 37.926</math></i>	$764.539 \pm 0.036$ <i><math>\pm 22.187</math></i>	$17.75 \pm 0.64$ <i><math>\pm 2.96</math></i>
	<b>3:</b>	$3500.282 \pm 0.103$ <i><math>\pm 14.089</math></i>	$285.691 \pm 0.009$ <i><math>\pm 1.150</math></i>	$9.81 \pm 0.64$ <i><math>\pm 1.46</math></i>
2009	<b>1:</b>	$1193.327 \pm 0.021$ <i><math>\pm 0.019</math></i>	$837.994 \pm 0.015$ <i><math>\pm 0.014</math></i>	$28.97 \pm 0.69$ <i><math>\pm 0.91</math></i>
	<b>2:</b>	$980.043 \pm 0.040$ <i><math>\pm 6.781</math></i>	$1020.363 \pm 0.042$ <i><math>\pm 7.061</math></i>	$14.53 \pm 0.68$ <i><math>\pm 1.50</math></i>
	<b>3:</b>	$1343.156 \pm 0.046$ <i><math>\pm 11.537</math></i>	$744.515 \pm 0.025$ <i><math>\pm 6.396</math></i>	$13.02 \pm 0.69$ <i><math>\pm 2.07</math></i>
	<b>4:</b>	$2453.043 \pm 0.047$ <i><math>\pm 0.049</math></i>	$407.657 \pm 0.008$ <i><math>\pm 0.009</math></i>	$11.54 \pm 0.68$ <i><math>\pm 0.77</math></i>
	<b>5:</b>	$3643.886 \pm 0.068$ <i><math>\pm 0.066</math></i>	$274.432 \pm 0.005$ <i><math>\pm 0.005</math></i>	$8.32 \pm 0.68$ <i><math>\pm 0.64</math></i>
2010	<b>1:</b>	$1395.980 \pm 0.0050$ <i><math>\pm 0.0056</math></i>	$716.334 \pm 0.0025$ <i><math>\pm 0.0029</math></i>	$28.76 \pm 0.48$ <i><math>\pm 0.62</math></i>
	<b>2*:</b>	$1412.9989 \pm 0.0068$ <i><math>\pm 0.0111</math></i>	$707.7141 \pm 0.0034$ <i><math>\pm 0.0055</math></i>	$15.01 \pm 0.48$ <i><math>\pm 0.47</math></i>
	<b>3*:</b>	$1370.5606 \pm 0.0086$ <i><math>\pm 0.0064</math></i>	$729.6288 \pm 0.0046$ <i><math>\pm 0.0034</math></i>	$14.44 \pm 0.45$ <i><math>\pm 0.45</math></i>
	<b>4:</b>	$2805.1524 \pm 0.0068$ <i><math>\pm 0.0075</math></i>	$356.4872 \pm 0.0009$ <i><math>\pm 0.0010</math></i>	$10.86 \pm 0.38$ <i><math>\pm 0.47</math></i>
	<b>5*:</b>	$1317.7424 \pm 0.0107$ <i><math>\pm 0.0100</math></i>	$758.8736 \pm 0.0062$ <i><math>\pm 0.0058</math></i>	$8.57 \pm 0.39$ <i><math>\pm 0.44</math></i>
	<b>6*:</b>	$1457.8933 \pm 0.0087$ <i><math>\pm 0.0093</math></i>	$685.9213 \pm 0.0042$ <i><math>\pm 0.0045</math></i>	$7.89 \pm 0.43$ <i><math>\pm 0.51</math></i>
	<b>7:</b>	$2180.7316 \pm 0.0135$ <i><math>\pm 0.0147</math></i>	$458.5617 \pm 0.0029$ <i><math>\pm 0.0031</math></i>	$5.50 \pm 0.38$ <i><math>\pm 0.40</math></i>

Note.\* Multiplet best-fitting periodicities (also marked on its FT) that were required to remove the signal from the FT to approximately  $\lesssim 4\sigma$ .

companions in wide orbits through a search for periodic variations in the arrival time of these pulsations (Mullally et al. 2008; Hermes 2018).

## 4.2 Near-IR wavelengths

We observed GD 1400 using Son OF Issac (SOFI; Moorwood, Cuby & Lidman 1998) on the New Technology Telescope La Silla on the nights of 2007 October 25 and 2007 October 26 as part of programme 080.C-0587(A). Photometry was obtained in the  $J$ ,  $H$ , and  $K_s$  filters using a five-point dither pattern with exposure times of 4 s for  $JH$  and 9 s for  $K_s$ . The seeing was between 0.5 and 1.6 arcsec.

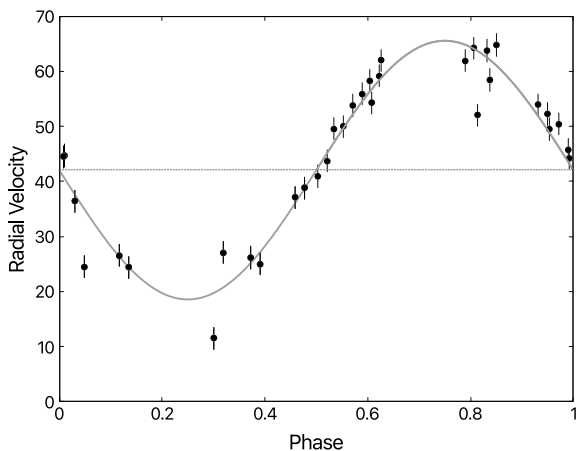


**Figure 3.** UVES RV measurements of GD 1400 folded on the best-fitting 9.98 h period.

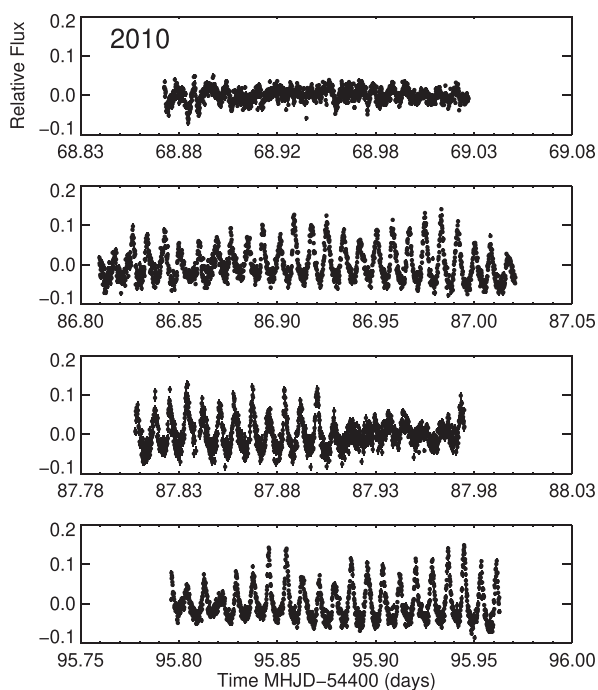


**Figure 4.** Light curves of GD 1400 taken in 2010 at SAAO with the UCT high-speed CCD in white light. The multiperiodic variable nature of GD 1400 (behaviour indicative of large-amplitude ZZ Ceti white dwarfs) is clearly evident. The light curve is expressed in terms of flux relative to the star’s mean brightness. Time is given in units of modified heliocentric Julian day (MHJD).

The data were reduced using the STARLINK software package ORAC-DR to perform the flat-fielding, sky subtraction, and mosaic combining each five dithered frames using the method outlined in Casewell et al. (2015). Object extraction was performed using aperture photometry routines within SEXTRACTOR and an aperture equivalent to the seeing.

There are 22 *J*-band, 22 *H*-band, and 23 *K<sub>s</sub>*-band data points after reduction (Fig. 6) covering phases 0–0.1, 0.4–0.55, and 0.65–0.77. The maxima and minima of the orbit are covered; however, there is no reflection effect detected similar to that seen in WD0137–349AB

(Casewell et al. 2015; Zhou et al. 2022), which is perhaps to be expected from the longer orbital period and cooler host star.

### 4.3 Mid-IR wavelengths

GD 1400 has been observed by NASA’s Wide Infrared Survey Explorer (*WISE*) mission (Wright et al. 2010; Mainzer et al. 2011) and there is archival time-series photometry from *ALLWISE* at both *W1* and *W2* (3.6 and 4.5 microns). The *ALLWISE* source catalogue (combined photometry) has  $13.801 \pm 0.026$  and  $13.633 \pm 0.033$ , respectively, for magnitudes in *W1* and *W2*, broadly consistent with the  $13.65 \pm 0.06$  and  $13.68 \pm 0.06$  determined by Farihi et al. (2005a) (it should be noted here that the *Spitzer* and *WISE* bands are not identical).

We used the *ALLWISE* guidance notes and removed all photometry flagged as affected by the moon, and those flagged as poor quality, or close to the South Atlantic Anomaly. For each data band, we performed a sinusoidal curve fit to the phase-folded data, keeping the period as a fixed parameter (Fig. 7). We calculated the chi-squared metric between the best-fitting sinusoid and the data, as well as a chi-squared metric between the data and a flat line at the mean value. From this comparison, we find that the reduced chi-squared value in *W1* is 28.05 for a sine and 31.33 for a flat value. So, *W1* is 1.12 times more likely to follow a sinusoidal trend than a flat line, which is not a statistically significant result. For *W2*, we find that the reduced chi-squared value is 9.91 for a sine and 30.79 for a flat line and that the data are 2.92 times more likely to follow a sinusoidal trend than the flat line at the mean of 13.69 mag. Therefore, the *W2* band shows a small reflection effect with semi-amplitude of 0.07 mag. This reflection effect is smaller than that detected for WD0137–349B, which has a semi-amplitude of 0.34 mag at 4.5 microns. NLTT5306B, however, which has a 101 min orbit, has a 4.5 micron reflection effect half that seen for GD 1400 at 0.047 mag. GD 1400 receives 9000 times less irradiation than WD0137–349B, and 320 times less than NLTT5306B. The reason for this difference may be clouds. As an L6–7 dwarf, GD 1400B is predicted to be more cloudy than the L5 NLTT5306B (Casewell et al. 2020b).

We interpolated the DA white dwarf models in the *WISE* filters from Tremblay, Bergeron & Gianninas (2011) for an 11 900 K,  $\log g = 8.0$  white dwarf to obtain apparent magnitudes of  $W1 = 15.325$  and  $W2 = 15.39$ . We subtracted the predicted white dwarf *W2* magnitude from the maximum and minimum measured by *ALLWISE* and calculated the brightness temperatures as described in Casewell et al. (2015) using the orbital separation of 0.009 au and a brown dwarf radius of  $0.086 R_{\odot}$ . This gives brightness temperatures of  $1760 \pm 10$  K for the nightside and  $1860 \pm 10$  K for the dayside. If we use a larger secondary radius, such as might be expected for an  $80 M_{\text{Jup}}$  object, then the temperatures drop to  $\sim 1550$  K on the nightside and  $\sim 1650$  K on the dayside. These brightness temperatures are just about consistent with those suggested by an L6–L7 dwarf. From observations of field L dwarfs, Dupuy & Liu (2017) give the effective temperature of L6–L7 dwarfs as between 1441 and 1615 K. An 1850 K dwarf would have a spectral type nearer to an L2–L3 dwarf using the same relationships.

Using the predicted magnitudes from Dupuy & Liu (2012) for L6–7 dwarfs, we get  $14.35 \pm 0.37$  and  $14.07 \pm 0.37$  as the combined white dwarf + brown dwarf magnitudes of the system, just consistent with the *ALLWISE* photometry on the nightside of the brown dwarf at 4.5 microns. The measured 3.6 micron magnitudes are, however, too bright by  $\sim 0.5$  mag, even taking into account the large scatter on the Dupuy & Liu (2012) magnitudes and the data. The spectral type would need to be nearer to L3–L4 to be consistent with these values.

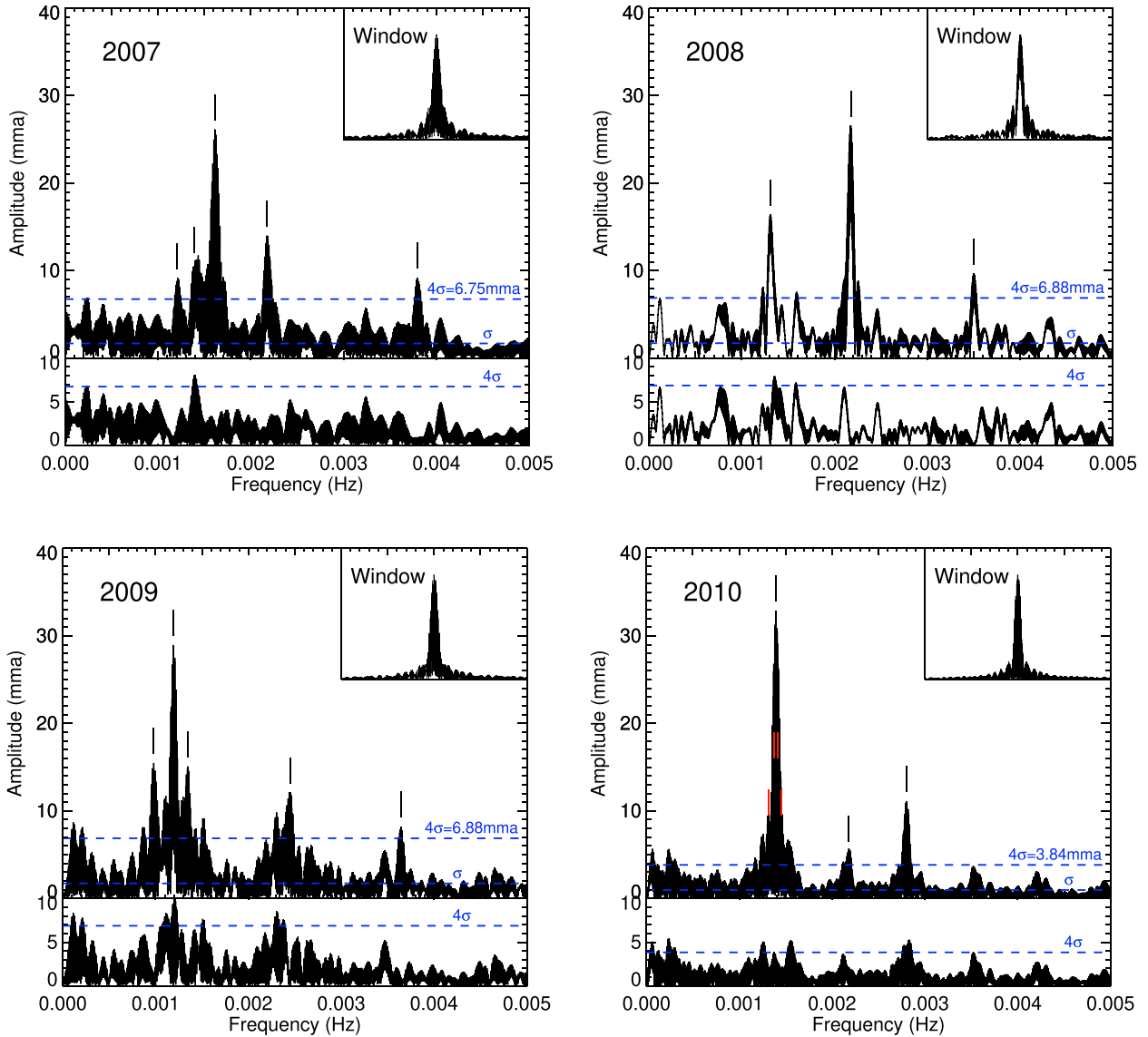


**Figure 5.** The upper panel for each epoch of data is the FT, as calculated using Period04, where the frequencies of the pulsation modes are marked with lines. The blue, dashed lines indicate the  $\sigma$  and  $4\sigma$  noise levels. The lower panel is the prewhitened FT on the same y-axis scale obtained after subtracting the indicated frequencies. The window function is given in each case. The red marks on the 2010 FT indicate multiplet best-fitting periodicities. Amplitude is given in units of milli-modulation amplitude (mma), where 10 mma is equivalent to 1 per cent.

Farihi et al. (2005a) suggested that the [3.6]–[4.5] mag colour of GD 1400B is too blue when compared to a L5–L7 dwarf, suggesting that there is significant absorption in the [4.5] band due to CO, although this result does not take into account the fact that there is photometric variability at 4.5 microns. These *Spitzer* data were taken at phases  $\sim 0.15$ – $0.18$  covering a very small part of the orbit as the reflection effect is reaching its maximum. Our *W1*–*W2* colour varies from 0.36 to  $-0.05$  mag, the latter of which is consistent with the Farihi et al. (2005a) values.

## 5 DISCUSSION

UVES RV measurements presented here reveal that the white dwarf + L6–L7 brown dwarf GD 1400AB has an orbital period  $P_{\text{orb}} = 0.4158$  d = 9.98 h and a separation  $a = 0.009$  au. The envelope of

the post-main-sequence progenitor would have extended beyond this distance, so GD 1400B must have survived a phase of CE evolution.

### 5.1 The mass of the brown dwarf

As our UVES spectra of GD 1400 are single lined, we can only determine a lower limit on the mass of GD 1400B from our spectroscopic data. The lack of any features (emission or absorption) from the brown dwarf in the majority of the UVES spectra means that we can only make RV measurements for the white dwarf.

Using the  $K$  velocities of  $21.8 \pm 1.1$  and  $199.2 \pm 0.6$  km s $^{-1}$  presented in Walters et al. (2023), which are consistent with our values for the white dwarf, and our updated mass for GD1400A, we derived a brown dwarf mass of  $0.074 \pm 0.007 M_{\odot}$  equating to  $78 \pm 6 M_{\text{Jup}}$ .

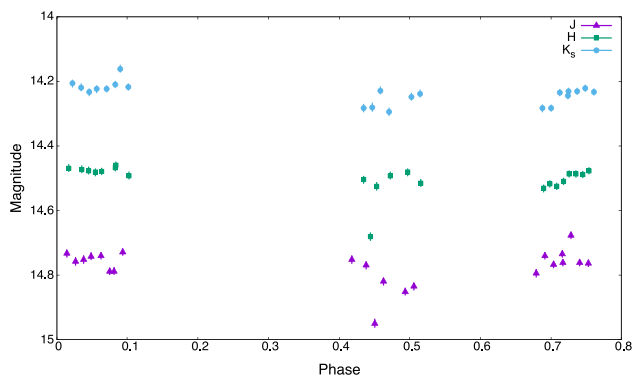


**Figure 6.** *J* (purple triangles), *H* (green boxes), and *K<sub>s</sub>* (blue circles) photometry phase-folded on the orbital period of GD1400AB. No significant variability due to a reflection effect is detected, although the orbital sampling is poor.

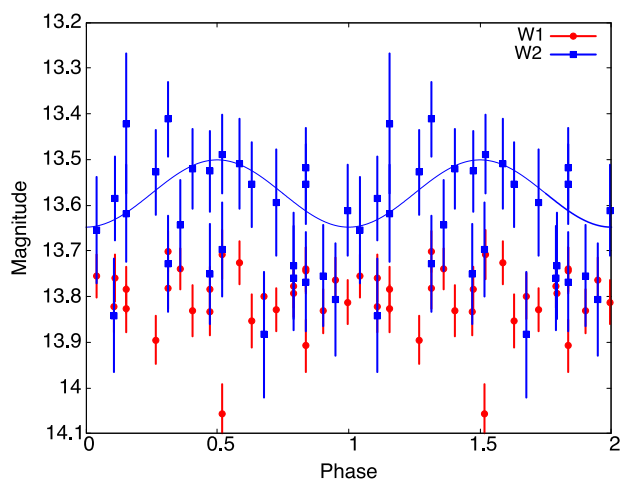


**Figure 7.** *ALLWISE* light curve for W1 (red circles) and W2 (blue boxes) phase-folded on the system period showing a reflection effect in the W2 band and the best-fitting sine curve (blue).

If we simply use our own  $K_1$  value for the white dwarf, then from Kepler’s laws and using the white dwarf mass estimate, the orbital period and our measured white dwarf’s velocity  $K_1 = 24.08 \pm 0.96 \text{ km s}^{-1}$  ( $=V_{\text{WD}}$ ), we determine the brown dwarf mass to be  $M_2 = 0.0812 \pm 0.0089 M_{\odot}$  if we use the inclination of  $60 \pm 10^\circ$  (Walters et al. 2023). At the higher end of the inclination ( $70^\circ$ ), but not large enough to eclipse, the secondary mass decreases to  $0.071 M_{\odot}$ . Both these mass estimates are large for a substellar object. Indeed, the spectral type of the brown dwarf (GD 1400B) has been constrained by two near-IR spectroscopic observations (Farihi & Christopher 2004; Dobbie et al. 2005) and additional *Spitzer* mid-IR photometry (Farihi et al. 2005a) to be L6–7. From observations of field L dwarfs, Dupuy & Liu (2017) give the effective temperature of L6–L7 dwarfs as between 1441 and 1615 K. At an age of 2 Gyr, the Sonora Bobcat (Marley et al. 2021) models predict that the brown dwarf mass should be between 0.058 and  $0.065 M_{\odot}$ . At the lowest end of our age limit, this is  $0.048\text{--}0.055 M_{\odot}$ , and at 6 Gyr it is  $0.069\text{--}0.071 M_{\odot}$ . It should be noted that the rms scatter on the Dupuy & Liu (2017) relationship between  $T_{\text{eff}}$  and spectral type is  $\sim 80 \text{ K}$ ; however, taking this into account, and the mass derived from the RVs, this would suggest an age for GD 1400AB of greater than 3 Gyr.

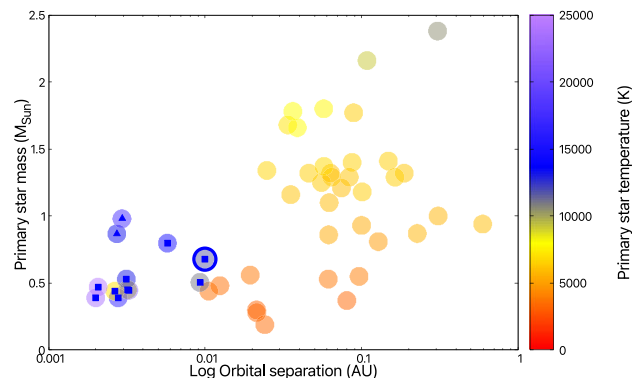


**Figure 8.** Brown dwarfs occupying the region known as the brown dwarf desert. Transiting brown dwarfs (Henderson et al. 2024) orbiting main-sequence stars as well as the known close, detached white dwarf–brown dwarf binaries (filled squares), and CVs (filled triangles) are shown comparing the primary masses, effective temperatures, and orbital separations. GD 1400AB is outlined with a circle.

If GD 1400B is indeed only 2 Gyr old as we determine from *WDWARFDATE*, then it may have had its cooling slowed by the influx of irradiation from GD 1400A, similar to the suggestions for NLTT5306AB (Casewell et al. 2020b; Amaro et al. 2023), or indeed be inflated such as WD1032+011B (Casewell et al. 2020a). This scenario would also possibly explain the mismatch between the proposed spectral type and the best-fitting model as determined by the *K*-band spectra in Walters et al. (2023), where the model is  $\sim 600 \text{ K}$  hotter than would normally be assumed for an L6–L7 dwarf. Alternatively, both WD0137–349B (Casewell et al. 2015) and SDSS1411 (Casewell et al. 2018b) have been shown to be too bright on both the dayside and nightside in the *K* band when compared to models of unirradiated brown dwarfs, and this may indeed be the same effect.

## 5.2 A possible evolutionary history for GD 1400

Even if the mass of the white dwarf GD 1400A is as much as  $0.1 M_{\odot}$  lower than the spectroscopically determined value of  $0.68 M_{\odot}$ , it is still around the peak of the mass distribution for field white dwarfs (Tremblay et al. 2016) and is most likely a C/O-core degenerate. Thus, the progenitor star likely underwent two giant phases, as would be expected for an isolated field white dwarf. Our progenitor mass as determined by *WDWARFDATE* is  $2.09^{+0.49}_{-0.52} M_{\odot}$  assuming single-star evolution.

Assuming solar metallicity, Hurley, Pols & Tout (2000) estimate the radius of a  $2.5 M_{\odot}$  red giant branch (RGB) star as  $25 R_{\odot}$  or  $0.12 \text{ au}$ , and the radius of a  $2.5 M_{\odot}$  asymptotic giant branch (AGB) star as  $250 R_{\odot}$  or  $1.2 \text{ au}$ . Therefore, during the main sequence phase GD 1400B must have orbited its parent star at a separation somewhere between  $\approx 0.1$  and  $1 \text{ au}$ . Interestingly, this region is precisely that which is largely void of brown dwarfs around solar-type main-sequence stars (Grether & Lineweaver 2006; Triaud et al. 2017). While only  $\sim 40$  transiting brown dwarfs have been discovered in this region (e.g. Henderson et al. 2024), coined the brown dwarf desert (Fig. 8),  $\sim 8$  per cent are orbiting stars more massive than  $2 M_{\odot}$  (Grievae et al. 2021; Psaridi et al. 2022; Vowell et al. 2023), although none of these are giants. Similarly, RV searches at first ascent giant stars, which are descended from the intermediate-mass stars that are the progenitors of white dwarfs such as GD 1400, find brown dwarfs orbiting within a few au at roughly the same frequency as for solar-

type stars (<1 percent; Hatzes et al. 2005; Lovis & Mayor 2007; Liu et al. 2008), and candidate substellar companions to red giants have been identified as causing long secondary period variability (Soszyński et al. 2021).

The details of the CE interaction following contact with the expanding AGB envelope are poorly understood, but it is thought that the drag on the brown dwarf forces it to quickly spiral in towards the core of the AGB star. The deposition of orbital energy as kinetic energy in the envelope causes it to be ejected from the system, leaving a close binary consisting of the AGB core (now a white dwarf) and the brown dwarf (e.g. Izzard et al. 2012).

In order to test this evolutionary pathway, we have reconstructed the CE phase using the same method recently used by Zorotovic & Schreiber (2022) for similar systems. This algorithm, developed by Zorotovic et al. (2010), searches for possible white dwarf progenitors in a grid of stellar evolution tracks generated with the single-star evolution (SSE) code from Hurley et al. (2000). Assuming that the core mass of the progenitor when it filled the Roche lobe is equal to the mass of the current white dwarf, we used the radius of the progenitor and the companion mass, assuming Roche geometry, to determine the period the system had at the onset of the CE phase for each possible progenitor. We then used the *energy formalism* for CE developed by Webbink (1984) with the binding and orbital energy calculated as in the binary-star evolution (BSE) code from Hurley, Tout & Pols (2002). The CE efficiency  $\alpha_{\text{CE}}$  was left as a free parameter, while the structural parameter  $\lambda$  was calculated as in Claeys et al. (2014) without considering contributions from recombination energy. The metallicity was set to  $z = 0.02$ . For the calculation of the final orbital energy, we used the period the system had when it emerged from the CE, which was calculated based on the current orbital configuration and the cooling time of the white dwarf, assuming gravitational radiation during the post-CE phase (Schreiber & Gänsicke 2003).

In Fig. 9, we show the total age of the system (top), i.e. the time until the CE phase occurred plus the cooling age of the white dwarf, and the progenitor mass (bottom) as a function of the CE efficiency  $\alpha_{\text{CE}}$  derived from our reconstruction. The results in dark grey were computed assuming a white dwarf mass consistent with our estimation. Considering the different values reported in the literature for the white dwarf mass, we allowed the progenitor’s core to vary between 0.6 and 0.7  $M_{\odot}$ . The mass of the companion was set to 0.0812  $M_{\odot}$  based on our estimation derived from the velocity ratio reported by Walters et al. (2023). We were able to reconstruct the CE phase without the need of recombination energy and with a small efficiency (as low as  $\alpha_{\text{CE}} \sim 0.35$ ), especially if the system is at least 2 Gyr old. Our reconstruction predicts an initial progenitor mass in the range of  $\sim 1.83\text{--}2.86 M_{\odot}$  and a total age of  $\sim 1\text{--}2.2$  Gyr, with all possible progenitors being on the AGB phase at the onset of the CE evolution. When restricting  $\alpha_{\text{CE}} \leq 0.41$ , to align with the range derived by Zorotovic & Schreiber (2022) for similar systems, the ranges for the possible mass of the progenitor and total age of the system are reduced to  $\sim 1.83\text{--}2.0 M_{\odot}$  and  $\sim 1.95\text{--}2.2$  Gyr, respectively. While the reconstructed parameters presented in Fig. 9 correspond to a fixed metallicity ( $z = 0.02$ ), different metallicities were also tested. Although these results are not shown in the figure, a lower metallicity leads to faster evolution, allowing for possible progenitors with lower masses and less envelope mass to expel during the CE phase. This results in a lower minimum value for the reconstructed efficiency ( $\alpha_{\text{CE}}$ ).

We also tested our reconstruction using the white dwarf mass of  $0.590 \pm 0.005 M_{\odot}$  derived by Walters et al. (2023). These results are shown in light grey in Fig. 9. Again, only possible progenitors

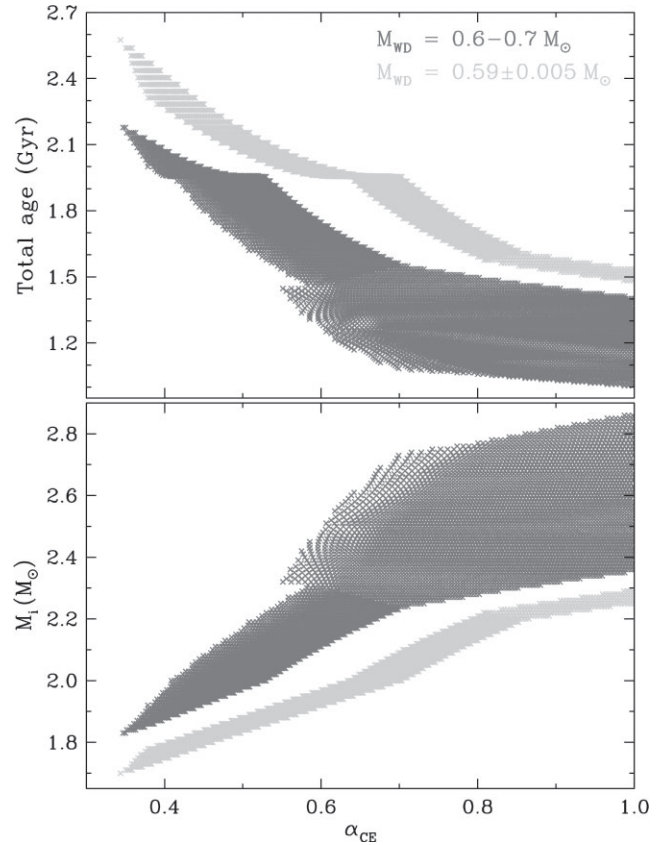


**Figure 9.** Total age of the system (top) and initial mass of the progenitor of the white dwarf (bottom) as a function of the CE efficiency  $\alpha_{\text{CE}}$  derived from our reconstruction. A fixed brown dwarf mass of 0.0812  $M_{\odot}$  was assumed. For the white dwarf mass, we consider two scenarios: one assuming a possible range of 0.6–0.7  $M_{\odot}$  (dark grey), and the other adopting  $0.590 \pm 0.005 M_{\odot}$  as derived by Walters et al. (2023) (light grey).

on the AGB phase are found, and the minimum value obtained for  $\alpha_{\text{CE}}$  remains as low as for a larger white dwarf mass. However, the reconstruction for a lower white dwarf mass predicts progenitors with lower initial masses, resulting in an older system compared to the case with the higher white dwarf mass derived here.

Finally, considering the uncertainty in the brown dwarf mass, we repeated the calculations assuming a mass at the lower end of our estimations, i.e. 0.071  $M_{\odot}$ . While the ranges for the possible initial mass of the progenitor and total age remained almost unchanged, we observed a slight shift towards larger values of the CE efficiency with a minimum value of  $\alpha_{\text{CE}} \sim 0.4$ . This behaviour is expected, as lowering the mass of the companion does not affect the possible progenitors of the white dwarf. However, it reduces the available orbital energy to eject the envelope, which translates in a larger CE efficiency required to emerge from the CE phase at a given orbital period.

If the CE phase had happened on the first ascent of the RGB phase, the growth of the progenitor’s core would have been significantly truncated. The premature ejection of the envelope during the RGB phase leaves behind a naked He core (<0.48  $M_{\odot}$ ). This core can ignite helium to become a hot subdwarf star, and later evolve into a hybrid He/CO white dwarf if the CE phase occurs near the tip of the RGB (Han et al. 2002; Arancibia-Rojas et al. 2024). Otherwise, if the naked core is not massive enough to ignite helium, it contracts and cools down after the CE ejection, becoming an He-core white



dwarf. This is most likely the evolutionary path for WD0137–349A, and the majority of the other known systems.

GD 1400 appears to have a different evolutionary history to many of the known close, detached white dwarf + brown dwarf binaries. Most of them contain white dwarfs with a mass  $<0.5 M_{\odot}$  (see table 1 in Zorotovic & Schreiber 2022). The WD0137–349AB system, for example, had the smaller original separation ( $\lesssim 0.1$  au) and underwent CE evolution on the RGB, while GD 1400B originally orbited its parent star at a wider separation, roughly between 0.1 and 1 au, and went through CE evolution only when its companion reached the AGB.

## 6 SUMMARY

RV measurements with UVES on the VLT conclusively demonstrate that the white dwarf + L6–L7 dwarf binary GD 1400 is a close system with an orbital period  $P_{\text{orb}} = 9.98$  h. Optical time-series photometry of GD 1400A shows that the pulsations are consistent with a large-amplitude ZZ Ceti variable and that the frequencies and amplitudes are unstable from year to year. *ALLWISE* photometry detects a weak reflection effect suggesting a day–night temperature difference of  $\sim 100$  K, but a nightside that is warmer than would be suggested by field dwarfs of the same spectral type, suggesting that either the system is younger, or the constant irradiation from the white dwarf has slowed the cooling of the brown dwarf. The brown dwarf must have survived a prior phase of CE evolution, when the progenitor of the white dwarf was on the AGB phase and not the RGB phase, making it different to the majority of the known systems.

## ACKNOWLEDGEMENTS

SLC acknowledges the support of an STFC Ernest Rutherford Fellowship ST/R003726/1. PB was supported in part by the NSERC Canada and by the Fund FQR-NT (Québec). JRF thanks the University of Leicester’s College of Science and Engineering for a PhD studentship. We thank Paul Dobbie for his input into the project. For the purpose of open access, the author has applied a Creative Commons Attribution (CC BY) licence to the Author Accepted Manuscript version arising from this submission. This paper is based on observations collected at the ESO, Paranal, Chile [programmes 077.D-0673(A) and 080.C-0587(A)], and observations made at the SAAO. This publication also makes use of data products from the *Wide-field Infrared Survey Explorer*, which is a joint project of the University of California, Los Angeles, and the Jet Propulsion Laboratory/California Institute of Technology, funded by the National Aeronautics and Space Administration.

## DATA AVAILABILITY

The UVES and SOFI data are available in the ESO data archive, and the *ALLWISE* data are public and available at IRSA. The SAAO data are available on request to the authors.

## REFERENCES

- Amaro R. C. et al., 2023, *ApJ*, 948, 129  
 Arancibia-Rojas E., Zorotovic M., Vučković M., Bobrick A., Vos J., Piraino-Cerda F., 2024, *MNRAS*, 527, 11184  
 Arcangeli J. et al., 2019, *A&A*, 625, A136  
 Beatty T. G., Marley M. S., Gaudi B. S., Colón K. D., Fortney J. J., Showman A. P., 2019, *AJ*, 158, 166  
 Bédard A., Bergeron P., Brassard P., Fontaine G., 2020, *ApJ*, 901, 93  
 Berger L., Koester D., Napiwotzki R., Reid I. N., Zuckerman B., 2005, *A&A*, 444, 565  
 Bergeron P., Dufour P., Fontaine G., Coutu S., Blouin S., Genest-Beaulieu C., Bédard A., Rolland B., 2019, *ApJ*, 876, 67  
 Bergeron P. et al., 2021, *AJ*, 162, 188  
 Bognár Z. et al., 2020, *A&A*, 638, A82  
 Bognár Z., Sódor Á., Clark I. R., Kawaler S. D., 2023, *A&A*, 674, A204  
 Brown A. J. et al., 2023, *MNRAS*, 521, 1880  
 Burleigh M. R., Hogan E., Dobbie P. D., Napiwotzki R., Maxted P. F. L., 2006a, *MNRAS*, 373, L55  
 Burleigh M. R. et al., 2006b, *MNRAS*, 373, 1416  
 Burleigh M. R. et al., 2011, in Schuh S., Drechsel H., Heber U., eds, AIP Conf. Proc. Vol. 1331, Planetary Systems Beyond the Main Sequence. Am. Inst. Phys., New York, p. 262  
 Casewell S. L. et al., 2015, *MNRAS*, 447, 3218  
 Casewell S. L. et al., 2018a, *MNRAS*, 476, 1405  
 Casewell S. L., Littlefair S. P., Parsons S. G., Marsh T. R., Fortney J. J., Marley M. S., 2018b, *MNRAS*, 481, 5216  
 Casewell S. L. et al., 2020a, *MNRAS*, 497, 3571  
 Casewell S. L., Debes J., Braker I. P., Cushing M. C., Mace G., Marley M. S., Kirkpatrick J. D., 2020b, *MNRAS*, 499, 5318  
 Claeys J. S. W., Pols O. R., Izzard R. G., Vink J., Verbunt F. W. M., 2014, *A&A*, 563, A83  
 Cummings J. D., Kalirai J. S., Tremblay P. E., Ramirez-Ruiz E., Choi J., 2018, *ApJ*, 866, 21  
 Dekker H., D’Odorico S., Kaufer A., Delabre B., Kotzłowski H., 2000, in Iye M., Moorwood A. F., eds, Proc. SPIE Conf. Ser. Vol. 4008, Optical and IR Telescope Instrumentation and Detectors. SPIE, Bellingham, p. 534  
 Dobbie P. D., Burleigh M. R., Levan A. J., Barstow M. A., Napiwotzki R., Holberg J. B., Hubeny I., Howell S. B., 2005, *MNRAS*, 357, 1049  
 Dupuy T. J., Liu M. C., 2012, *ApJS*, 201, 19  
 Dupuy T. J., Liu M. C., 2017, *ApJS*, 231, 15  
 Farihi J., Christopher M., 2004, *AJ*, 128, 1868  
 Farihi J., Zuckerman B., Becklin E. E., 2005a, *AJ*, 130, 2237  
 Farihi J., Becklin E. E., Zuckerman B., 2005b, *ApJS*, 161, 394  
 Fontaine G., Bergeron P., Billères M., Charpinet S., 2003, *ApJ*, 591, 1184  
 Fortney J. J., Lodders K., Marley M. S., Freedman R. S., 2008, *ApJ*, 678, 1419  
 Gentile Fusillo N. P. et al., 2021, *MNRAS*, 508, 3877  
 Gianninas A., Bergeron P., Ruiz M. T., 2011, *ApJ*, 743, 138  
 Girven J., Gänsicke B. T., Steeghs D., Koester D., 2011, *MNRAS*, 417, 1210  
 Grether D., Lineweaver C. H., 2006, *ApJ*, 640, 1051  
 Grieves N. et al., 2021, *A&A*, 652, A127  
 Han Z., Podsiadłowski P., Maxted P. F. L., Marsh T. R., Ivanova N., 2002, *MNRAS*, 336, 449  
 Hatzes A. P., Guenther E. W., Endl M., Cochran W. D., Döllinger M. P., Bedalov A., 2005, *A&A*, 437, 743  
 Henderson B. A. et al., 2024, *MNRAS*, 530, 318  
 Hermes J. J., 2018, in Deeg H. J., Belmonte J. A., eds, Handbook of Exoplanets. Springer, Cham, p. 6  
 Hermes J. J. et al., 2017, *ApJS*, 232, 23  
 Hernández Santisteban J. V. et al., 2016, *Nature*, 533, 366  
 Hurley J. R., Pols O. R., Tout C. A., 2000, *MNRAS*, 315, 543  
 Hurley J. R., Tout C. A., Pols O. R., 2002, *MNRAS*, 329, 897  
 Izzard R. G., Hall P. D., Tauris T. M., Tout C. A., 2012, in Proc. IAU Symp. 283, Planetary Nebulae: An Eye to the Future. Cambridge Univ. Press, Cambridge, p. 95  
 Kilkeny D., Welsh B. Y., Koen C., Gulbis A. A. S., Kotze M. M., 2014, *MNRAS*, 437, 1836  
 Kiman R., Xu S., Faherty J. K., Gagné J., Angus R., Brandt T. D., Casewell S. L., Cruz K. L., 2022, *AJ*, 164, 62  
 Knutson H. A. et al., 2012, *ApJ*, 754, 22  
 Koester D., 2010, Mem. Soc. Astron. Ital., 81, 921  
 Koester D., Dreizler S., Weidemann V., Allard N. F., 1998, *A&A*, 338, 612  
 Koester D., Voss B., Napiwotzki R., Christlieb N., Homeier D., Lisker T., Reimers D., Heber U., 2009, *A&A*, 505, 441  
 Lee E. K. H., Casewell S. L., Chubb K. L., Hammond M., Tan X., Tsai S.-M., Pierrehumbert R. T., 2020, *MNRAS*, 496, 4674

- Lenz P., Breger M., 2005, *Commun. Asteroseismology*, 146, 53
- Lew B. W. P. et al., 2022, *AJ*, 163, 8
- Littlefair S. P., Dhillon V. S., Marsh T. R., Gänsicke B. T., Baraffe I., Watson C. A., 2007, *MNRAS*, 381, 827
- Littlefair S. P. et al., 2014, *MNRAS*, 445, 2106
- Liu Y. J. et al., 2008, *ApJ*, 672, 553
- Longstaff E. S., Casewell S. L., Wynn G. A., Maxted P. F. L., Helling C., 2017, *MNRAS*, 471, 1728
- Lorenz R., Mayer P., Drechsel H., 1998, *A&A*, 332, 909
- Lothringer J. D., Casewell S. L., 2020, *ApJ*, 905, 163
- Lovis C., Mayor M., 2007, *A&A*, 472, 657
- McCarthy C., Zuckerman B., 2004, *AJ*, 127, 2871
- Mainzer A. et al., 2011, *ApJ*, 731, 53
- Marley M. S. et al., 2021, *ApJ*, 920, 85
- Maxted P. F. L., Napiwotzki R., Dobbie P. D., Burleigh M. R., 2006, *Nature*, 442, 543
- Metchev S. A., Hillenbrand L. A., 2009, *ApJS*, 181, 62
- Mikal-Evans T. et al., 2022, *Nat. Astron.*, 6, 471
- Moorwood A., Cuby J. G., Lidman C., 1998, *The Messenger*, 91, 9
- Mullally F., Winget D. E., Degennaro S., Jeffery E., Thompson S. E., Chandler D., Kepler S. O., 2008, *ApJ*, 676, 573
- Napiwotzki R., Edelmann H., Heber U., Karl C., Drechsel H., Pauli E.-M., Christlieb N., 2001, *A&A*, 378, L17
- Napiwotzki R. et al., 2004, in Hilditch R. W., Hensberge H., Pavlovski K., eds, *ASP Conf. Ser. Vol. 318, Spectroscopically and Spatially Resolving the Components of the Close Binary Stars*. Astron. Soc. Pac., San Francisco, p. 402
- Napiwotzki R. et al., 2020, *A&A*, 638, A131
- Parsons S. G. et al., 2017, *MNRAS*, 471, 976
- Patterson J., Thorstensen J. R., Kemp J., 2005, *PASP*, 117, 427
- Pinfield D. J., Jones H. R. A., Lucas P. W., Kendall T. R., Folkes S. L., Day-Jones A. C., Chappelle R. J., Steele I. A., 2006, *MNRAS*, 368, 1281
- Politano M., 2004, *ApJ*, 604, 817
- Psaridi A. et al., 2022, *A&A*, 664, A94
- Rappaport S. et al., 2017, *MNRAS*, 471, 948
- Rebassa-Mansergas A., Xu S., Raddi R., Pala A. F., Solano E., Torres S., Jiménez-Esteban F., Cruz P., 2022, *ApJ*, 927, L31
- Schreiber M. R., Gänsicke B. T., 2003, *A&A*, 406, 305
- Soszyński I. et al., 2021, *ApJ*, 911, L22
- Steele P. R., Burleigh M. R., Dobbie P. D., Jameson R. F., Barstow M. A., Satterthwaite R. P., 2011, *MNRAS*, 416, 2768
- Steele P. R. et al., 2013, *MNRAS*, 429, 3492
- Stevenson K. B. et al., 2014, *Science*, 346, 838
- Tremblay P. E., Bergeron P., Gianninas A., 2011, *ApJ*, 730, 128
- Tremblay P. E., Ludwig H. G., Steffen M., Freytag B., 2013, *A&A*, 552, A13
- Tremblay P. E., Cummings J., Kalirai J. S., Gänsicke B. T., Gentile-Fusillo N., Raddi R., 2016, *MNRAS*, 461, 2100
- Triaud A. H. M. J. et al., 2017, *A&A*, 608, A129
- van Roestel J. et al., 2021, *ApJ*, 919, L26
- Vanderburg A. et al., 2020, *Nature*, 585, 363
- Vincent O., Bergeron P., Lafrenière D., 2020, *AJ*, 160, 252
- Vowell N. et al., 2023, *AJ*, 165, 268
- Walters N., Farihi J., Marsh T. R., Breedt E., Cauley P. W., von Hippel T., Hermes J. J., 2023, *MNRAS*, 519, 1381
- Webbink R. F., 1984, *ApJ*, 277, 355
- Wright E. L. et al., 2010, *AJ*, 140, 1868
- Zhou Y. et al., 2022, *AJ*, 163, 17
- Zorotovic M., Schreiber M., 2022, *MNRAS*, 513, 3587
- Zorotovic M., Schreiber M. R., Gänsicke B. T., Nebot Gómez-Morán A., 2010, *A&A*, 520, A86

This paper has been typeset from a  $\text{\TeX}/\text{\LaTeX}$  file prepared by the author.